Soiling, Adhesion, and Surface Characterization of Concentrated Solar Power Reflectors Insights and Challenges in the MENA Region

El Baraka, Ayoub ; En-nadir, Redouane; Basyooni-M.Kabatas, Mohamed A.; Jorio, Anouar; Khaldoun, Asmae

DOI
10.3390/su16146257

Publication date
2024

Document Version
Final published version

Published in
Sustainability

sustainability

MDPI

Article

Soiling, Adhesion, and Surface Characterization of Concentrated Solar Power Reflectors: Insights and Challenges in the MENA Region

Ayoub El Baraka [1], Redouane En-nadir [1,*], Mohamed A. Basyooni-M. Kabatas [2,3,4,*], Anouar Jorio [1] and Asmae Khaldoun [5]

[1] Laboratory of Solid State Physics, Department of Physics, Faculty of Sciences Dhar El Mahraz, Sidi Mohamed Ben Abdellah University, Fez 30000, Morocco; ayoub.elbaraka@usmba.ac.ma (A.E.B.)
[2] Department of Precision and Microsystems Engineering, Delft University of Technology, Mekelweg 2, 2628 CD Delft, The Netherlands
[3] Department of Nanotechnology and Advanced Materials, Graduate School of Applied and Natural Science, Selçuk University, Konya 42030, Turkey
[4] Solar Research Laboratory, Solar and Space Research Department, National Research Institute of Astronomy and Geophysics, Cairo 11421, Egypt
[5] School of Science and Engineering, Al Akhawayn University, Ifrane 53000, Morocco
* Correspondence: redouane.en-nadir@usmba.ac.ma (R.E.-n.); m.kabatas@tudelft.nl or m.a.basyooni@gmail.com (M.A.B.-M.K.)

Abstract: Desert environments are prime locations for concentrated solar power (CSP) applications due to abundant direct normal irradiance. Despite this advantage, the accumulation and adhesion of dust on CSP mirror surfaces present significant challenges to plant efficiency. This paper comprehensively explores soiling phenomena and dust adhesion mechanisms, complemented by advanced measurement techniques tailored for CSP reflector mirrors. By elucidating the factors influencing dust accumulation and delving into the thermodynamics of self-cleaning coatings, alongside an analysis of various mirror materials, this study aims to enrich our understanding of soiling in CSP systems. This study aims to provide valuable insights that will help develop strategies to reduce dust-related efficiency losses in CSP plants, ultimately supporting the development of more reliable and sustainable solar energy solutions for the MENA region.

Keywords: soiling; concentrated solar power; dust adhesion; anti-soiling coating; reflector mirrors

Citation: El Baraka, A.; En-nadir, R.; Basyooni-M. Kabatas, M.A.; Jorio, A.; Khaldoun, A. Soiling, Adhesion, and Surface Characterization of Concentrated Solar Power Reflectors: Insights and Challenges in the MENA Region. *Sustainability* **2024**, *16*, 6257. https://doi.org/10.3390/su16146257

Academic Editor: Mariateresa Lettieri

Received: 30 May 2024
Revised: 22 June 2024
Accepted: 15 July 2024
Published: 22 July 2024

1. Introduction

In desert environments, soiling presents a significant issue that can impact the optical properties of solar panels [1]. Soiling encompasses dust adhesion and accumulation and various particles that can reduce energy yield by causing absorption and scattering losses of incident light, such as soot, salt, and bird droppings [2]. Soiling is a complex and challenging phenomenon to predict. Understanding it begins with defining dust particles and wind properties, then exploring dust grain behavior in the air and the interaction between sand movement and wind properties.

The first step involves studying the sedimentary composition of soils, which serve as the source material for sandstorms. Soil texture comprises mineral granular particles categorized by size and composition. According to the Wentworth grade scale, sand sizes range from 100 μm for fine particles to 2000 μm for very coarse particles [3]. Dust is defined as clay and silt particles with a diameter of less than 100 μm. Additionally, the forces affecting a single grain falling in the air gravity ($\vec{g}$) and air resistance ($\vec{R}$) are crucial considerations. These forces reach equilibrium, determining the grain's terminal velocity of fall [4]. Particle transportation modes, such as saltation or suspension, vary based on

size, shape, and wind velocity, with implications for solar panels' susceptibility to soiling, as shown in Figure 1 [5].

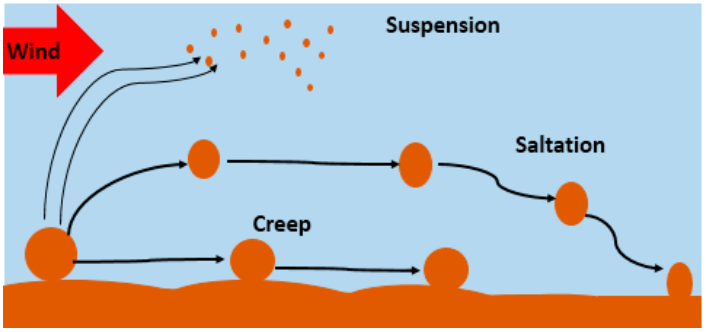

Figure 1. Schematic illustrating the various modes of particle transportation.

Similarly, as wind velocity increases, particles with a size of around 100 μm are the first to move [6]. According to Bagnold's research in 1941 [7], surface wind is the primary cause of dust removal, transportation, and deposition. The wind velocity at which saltation might occur is called the fluid threshold and can be expressed by the following equation:

$$\mathbf{u_{ft}} = \mathbf{A_{ft}}\sqrt{\frac{\rho_P - \rho_a}{\rho_a}\mathbf{g}\mathbf{D_P}} \quad (1)$$

where $\mathbf{A_{ft}}$ is the constant depending on the inter-particle forces, the lift force, and the Reynolds number, $\boldsymbol{\rho_P}$ is the density of the particle, $\boldsymbol{\rho_a}$ is the density of air, $\mathbf{g}$ is the gravitational acceleration, and $\mathbf{D_P}$ is the particle's diameter.

According to Shao and Lu [8], the Bagnold expression accurately captures the fluid threshold for particles larger than 100 μm. However, it does not predict a minimal fluid threshold at 75 μm and subsequent increase with decreasing particle size. Shao and Lu's revised fluid threshold expression takes into account the balance of driving and retarding forces (cohesion and gravity). It is assumed that cohesive force is related to particle size. As a result, the fluid threshold might be stated by the following equation:

$$\mathbf{u_{ft}} = \mathbf{A_{ft}}\sqrt{\frac{\rho_P - \rho_a}{\rho_a}\mathbf{g}\mathbf{D_P} + \frac{\gamma}{\rho_a D_P}} \quad (2)$$

where γ is the scaling factor for the interactive forces between particles.

In addition to defining soiling, the impact of soiling phenomena also hinges on the deposition rate. The rate at which the wind removes dust deposition correlates with the airborne dust concentration, as elaborated in the following section. Within our context, the mean wind speed in the MENA region exhibits variability but generally ranges between 3–8 m/s, with certain areas experiencing higher values. This variability in wind speeds significantly influences the region's potential for wind energy development, an endeavor actively pursued by several countries [9].

- Airborne dust concentration

Airborne dust concentration dust serves as the most reliable predictor of soiling. Previous research [8] revealed a strong correlation between soiling rates across different regions and the concentration of dust particles measuring 10 μm or less in diameter, as depicted in Figure 2. A strong correlation exists between the high maximum soiling rate and the annual mean airborne dust concentrations for particulate matter less than 10 μm across various regions. This finding is consistent with a global map depicting modeled annual median airborne dust concentrations for $PM_{2.5}$ in various regions, including North and West Africa, the Middle East, Asia, and East and Southeast Asia. These locations have a dry environment and little precipitation, as shown in Figure 3. The yearly median

concentration of $PM_{2.5}$, measured in micrograms per cubic meter, reveals information on regions with low and high PM dust concentrations.

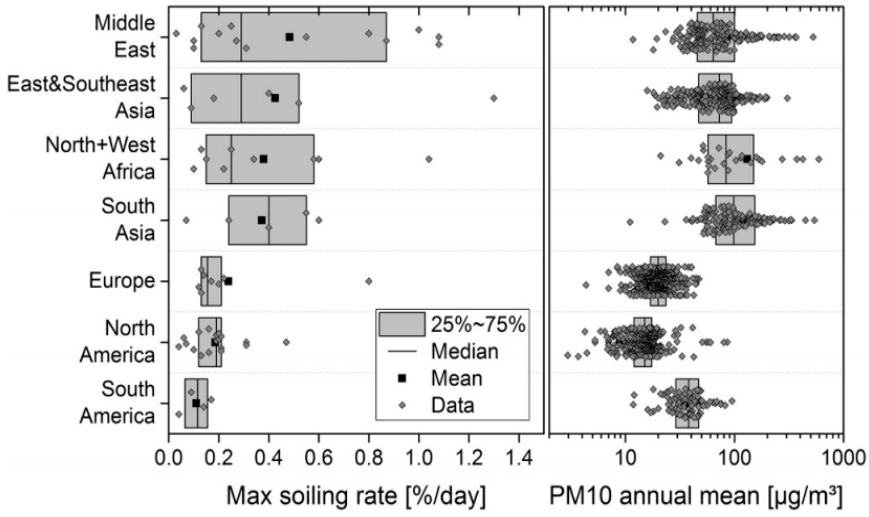

Figure 2. Maximum Daily Soiling Rates vs. Annual Mean Airborne Dust Concentrations of PM10 Across Various Regions.

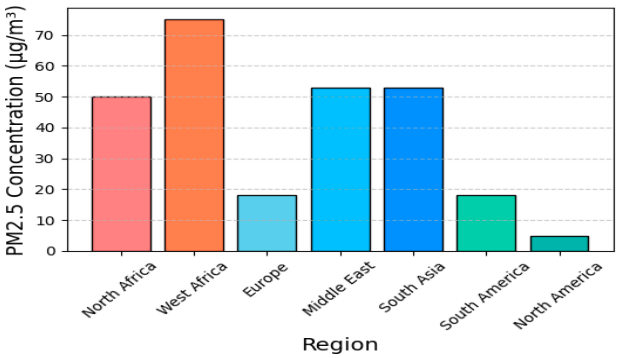

Figure 3. Concentration of $PM_{2.5}$ Across Different Regions, including the MENA region.

In addition to the impact of airborne dust on the performance of installed solar power (CSP) plants in the MENA region, the total CSP installed in the region is approximately 1 GW, contributing to the energy supply to achieve the renewable broad targets set by MENA countries [10].

- Factors Contributing to Dust Accumulation

Following monitoring airborne particulate matter with an aerodynamic diameter of less than 10 µm (PM_{10}) across various geographical regions, we aim to gain insight into the phenomena of soiling and the determinants influencing the deposition of dust particles on surfaces. Indeed, dust deposition is contingent upon four fundamental factors as illustrated in Figure 4: particulate composition, environmental conditions, geographical location, and structural characteristics [11]. The four factors affecting dust accumulation are interdependent. However, more dust accumulates over higher elevations. Additionally, faster winds correspond to lower pressures, reducing soil accumulation. It should be noted that the "Dust Characteristics" column in Figure 4 includes physical dust particles and biological contaminants such as bacteria. This classification highlights the types of contaminants that can affect CSP reflector performance and provides a detailed understanding of the pollution challenge.

Human activities and land-use changes can significantly alter dust sources and sediments, while vegetation cover and climate play an important role in dust storage and

transport. Industrial activity also contributes to generating airborne particulate matter, affecting local dust development. In our case, CSP plants, which are generally located in dry areas with high sunlight exposure, are exposed to severe weather conditions such as wind storms and sand/dust storms, which can reduce their specular reflection. Combining these studies aims to increase the scientific rigor of our findings and provide valuable insights for reducing dust exposure to solar power plants.

Environmental factors such as temperature, humidity, and wind velocity significantly impact dust adhesion dynamics on photovoltaic (PV) or reflector mirror surfaces. Elevated temperatures can increase surface energy and potentially reduce the effectiveness of hydrophobic coatings by altering their contact angle and adhesive properties. Conversely, lower temperatures may enhance surface hydrophobicity, potentially decreasing dust adhesion. Humidity levels also play a critical role; higher humidity can elevate moisture levels on solar surfaces, promoting dust adhesion through capillary forces. Furthermore, wind velocity affects the rate of dust particle deposition on solar panels. High wind speeds can increase the kinetic energy of dust particles, intensifying their impact force and adherence to surfaces, which may diminish the benefits of anti-soiling coatings.

These factors collectively influence the durability and performance of solar panels in dusty environments. By exploring these influences, our goal is to provide a comprehensive understanding of how environmental conditions shape dust adhesion dynamics and impact the effectiveness of mitigation strategies in CSP plants or PV technology.

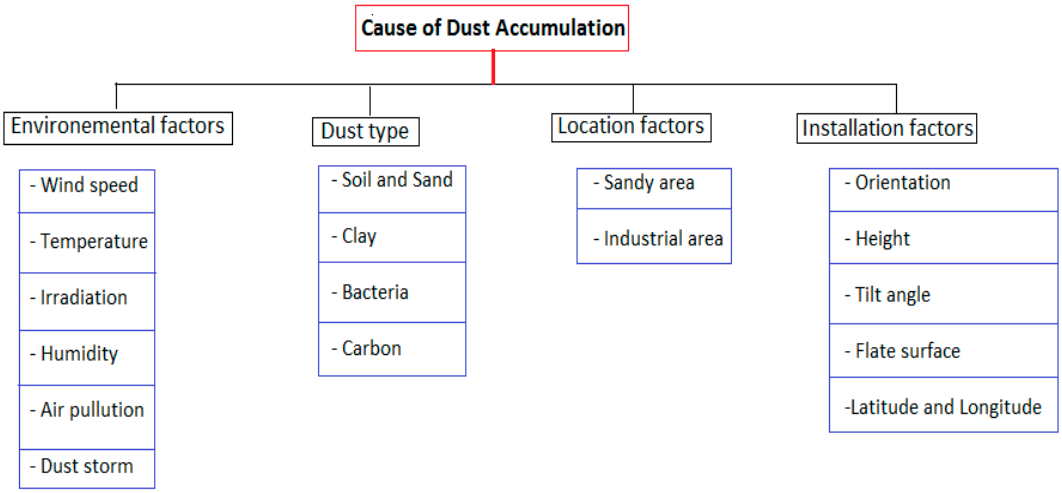

Figure 4. Factors Contributing to Dust Accumulation.

The implementation of CSP in the MENA region faces considerable challenges, including environmental and psychological constraints related to land availability and environmental impacts, the adoption of complex regulatory approaches through different countries, high upfront costs and special technical requirements, dynamic dynamics, increased economic profitability issues and price, and economic uncertainty. Effectively addressing these challenges requires concerted efforts by stakeholders to streamline regulation, enhance technical capacity, and establish strong financial incentives for sustainable CSP implementation in the MENA region.

2. Challenges Facing CSP Projects in the MENA Region

The arid climate of the MENA region poses significant environmental challenges to CSP projects, especially due to high levels of dust and sand causing extensive damage to CSP reflectors, reducing their productivity, while harsh conditions, including high

temperatures and sand storms, exacerbate these issues. Advanced, cost-effective cleaning and maintenance technologies are needed to improve performance and longevity.

Legal and economic challenges also present major obstacles. Regulatory frameworks across the MENA region are often complex and inconsistent, with lengthy approval processes and a lack of formalized processes that can delay project implementation. Furthermore, initial capital costs of CSP projects, financial instability and competition from expensive minerals and hedge funds, may restrict investment, which remains significant, and investors have to consider long payback periods and potential risks.

Technological, social, and political challenges further complicate the CSP project. Optimizing CSP technology to withstand harsh environmental conditions is important, but challenging. Public acceptance and awareness of CSP technologies may be low, requiring greater community engagement and educational efforts. Political instability in a region can disrupt project timelines and deter foreign investment, highlighting the need for a strong political will and concerted efforts to prioritize renewable energy initiatives in the region.

3. Measurement of Soil and Dust Adhesion on CSP Surfaces

In the world of solar energy, different methodologies exist for quantifying soiling on solar panels and, as a result, correlating energy yield losses. According to the literature, these techniques are grouped into four categories: measuring soil mass, analyzing solar module output, evaluating light transmission, and using outdoor microscopy to evaluate dust deposition.

- Soil mass and output of solar modules
- Dust deposition on the surface of solar panels can reduce the efficiency of solar modules. Al-Hasan et al. [12] observed that soil mass accumulates proportionally with transmission loss and the output of photovoltaic (PV) panels. Characterizing soiling by soil mass is thus an effective method to measure soiling, allowing the determination of the size, texture, and composition of adhering dust particles and estimation of the amount of incident radiation scattered and absorbed. In addition to soil mass, the performance of PV panels is directly related to incident light affected by soil mass accumulation. Solar module output can be assessed using the soiling ratio, as described by the IEC 61724-1 standard [13], which calculates the short-circuit current of the soiled sample over that of the clean sample:

$$\boldsymbol{r_S(t)=\frac{I_{SC_{soil}}(t)}{I_{SC_{ref}}(t)}} \quad (3)$$

where $\boldsymbol{I_{SC_{soil}}(t)}$ and $\boldsymbol{I_{SC_{ref}}(t)}$ represent the short-circuit currents of the soiled and clean reference solar samples, respectively. In the context of CSP reflector mirrors, various portable instruments are employed to measure reflectance and assess energy yield losses due to soiling. These instruments include devices such as the Abengoa Condor SR-6.1 portable reflectometer, which measures reflectance in CSP mirrors [13]. Additionally, custom reflectometers have been developed to capture images of mirror contaminants and perform quasi-monochromatic reflectivity loss measurements [14].

A custom reflectometer based on a commercial Digital Single Lens Reflex (DSLR) camera is illustrated in Figure 5. The loss of reflectance of a mirror due to the momentum and kinetic energy of the dust particles is presented in the equation developed by Barrier and Collier (1980) [15]:

$$\boldsymbol{L = K + A \times \sigma \times \vartheta + B \times \sigma \times \vartheta^2} \quad (4)$$

$\boldsymbol{K}$ is a constant representing noise unrelated to dust abrasion, $\boldsymbol{\sigma}$ corresponds to the dust mass per unit area, $\boldsymbol{A}$ and $\boldsymbol{B}$ are empirical regression variables, and $\boldsymbol{\vartheta}$ represents the wind velocity.

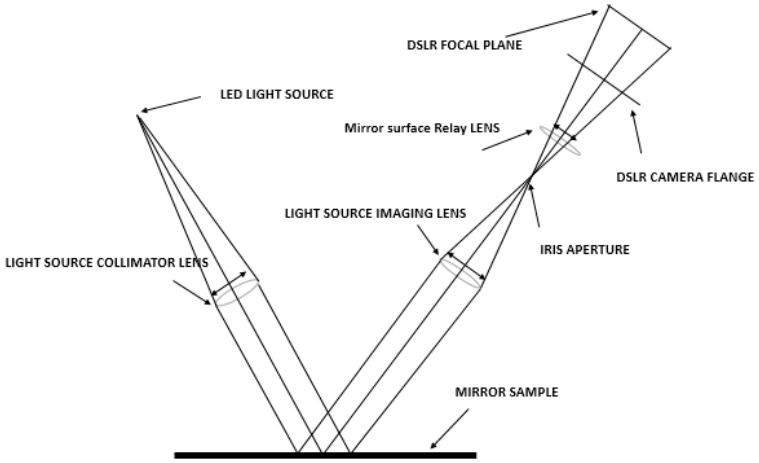

Figure 5. Optical Layout of the DSLR-Based Contamination Camera.

3.1. Light Transmission

In the literature [16,17], soiling can be characterized by light transmission through the glass substrate. In the context of photovoltaic (PV) performance, the soiling transmission loss of solar panel samples can be quantified using a pyranometer or spectrometer. This measurement compares the transmission of light through clean versus soiled samples. The dust particles tend to selectively attenuate shorter wavelengths of light, leading to a slight red-shift in the transmitted light.

- Outdoor soiling microscopy

Soiling measurements can also be quantified using an effective technique based on images of soiled samples obtained from outdoor soiling microscopy [18]. The microscope, developed by the Environment and Energy Research Institute group in Qatar, comprises a small, low-power digital microscope connected to a Raspberry Pi3. The microscope features a glass slide with a surface area of 4.40 mm^2 for soiling collection, and the resolution of the captured images is 0.935 μm/pixel. The microscope can capture images of the soiled samples and transfer them to ImageJ software (1.53) to calculate the percentage of dust accumulation.

3.2. Dust Accumulation on CSP Reflector Surfaces

Reflector mirrors are essential components of solar power systems, and dust and dirt accumulation can adversely affect their efficiency. To mitigate this issue, various anti-soiling coatings are applied to the mirrors. Techniques are available to measure dust outdoadhesion and assess its impact on mirror performance. Research has investigated various reflector mirror designs within solar power systems, each offering unique advantages. These studies emphasize the enhancement of durability and efficiency through advanced coatings and measurement methods.

- Surface Mirror

Front-surface mirrors have a metallic coating on the front, which causes incoming light to reflect directly off the top layer. As demonstrated in Figures 6 and 7, these mirrors are prone to soiling, which can significantly reduce their specular reflection. In contrast, in second-surface mirrors, the metallic coating is put to the back of a transparent material, usually glass. This design improves the adherence of the reflective film [19], making it more robust and soil-resistant [20].

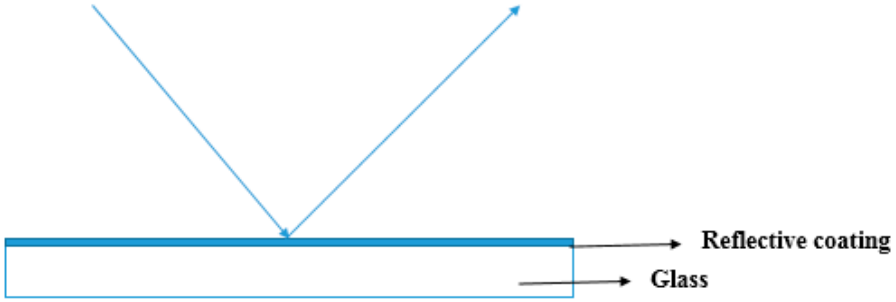

Figure 6. First-surface mirror structures.

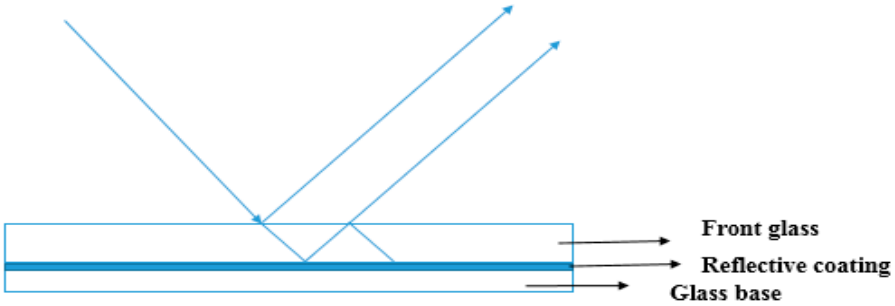

Figure 7. Second-surface mirror structures.

As component materials, most reflector mirrors are made from silver or aluminum as reflecting surfaces. Silver is known for its high reflectance, flexibility, and lightweightness compared to aluminum. However, the cost of silver reflecting mirrors is significantly higher. Silver mirrors have a shorter lifespan due to aging caused by the low adhesion between the silver coating and the polymer substrate [21].

The most important characteristic for CSP plants is the specular reflectance (S.R.) of the mirrors. The incident light can be either reflected, transmitted, or absorbed, as indicated in the formula below:

$$\boldsymbol{R + T + A = 1} \quad (5)$$

The type of reflectance of the mirrors depends on the surface type: specular reflectance for smooth surfaces or diffuse reflectance for rough surfaces [22]. On a soft surface, the surface is specular if the incident irradiation is reflected with the same magnitude and intensity. However, when the incident beam is uniformly reflected in all directions on a rough surface, the surface is diffuse, as illustrated in the following Figure 8 [23]. The specular and diffuse reflectance are essential parameters for accurately characterizing mirrors. Regarding the types of CSP reflector mirror materials, three main types are available in the literature: second-surface silvered glass, silvered polymer mirrors, and aluminum mirrors.

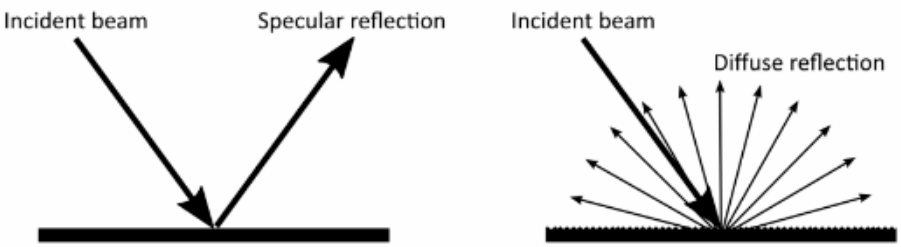

Figure 8. Comparison of Specular Reflectance and Diffuse Reflectance.

- Second-surface Silvered Glass Mirrors

Second-surface silvered glass mirrors are obtained by applying silver to the back surface of the glass, as depicted in Figure 9. To reduce double absorption when incident light is transmitted, the thickness of the glass typically ranges from 1 to 4 mm. As noted in [24], two main types of second-surface silvered glass mirrors are distinguished: thin glass, when the silver coating is less than 1 mm thick, and thick glass, when the silver layer is approximately 4 mm thick. Additionally, various coatings are applied to protect the silver coating from degradation, as illustrated in the following figure.

Figure 9. Second-surface silvered glass.

- Silvered Polymer Mirrors

Silvered polymer mirrors are obtained by applying a polymer film to the reflective metal layer coated with an adhesive and substrate material, as shown in Figure 10 [25]. The polymer film, typically Poly-methyl-methacrylate (PMMA), is characterized by its high transmittance and ability to resist damage and UV radiation. Compared to second-surface silvered glass mirrors, silvered polymer mirrors are more flexible and cheaper.

- Aluminum Mirrors

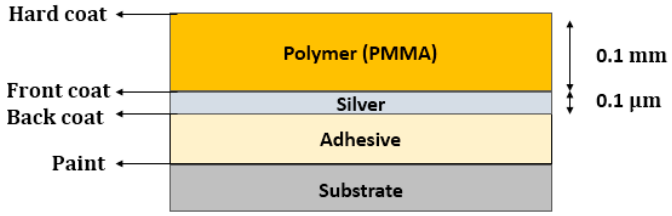

Figure 10. Silvered Polymer Mirrors.

The structure of aluminum mirrors consists of an aluminum film deposited on a polished aluminum surface and protected from damage by applying silica oxidation coatings [26], as illustrated in Figure 11. Generally, aluminum mirrors are used in CSP Fresnel collectors or solar cookers due to their flexibility in application.

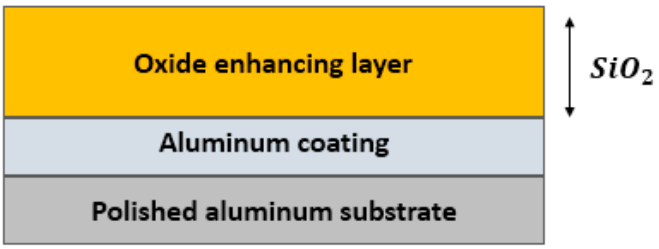

Figure 11. Aluminum mirrors.

4. Anti-Soiling Coating and Thermodynamics of Self-Cleaning Coating

CSP reflector plants are typically situated in arid regions where direct normal irradiation (DNI) is significant. However, harsh environmental conditions in these regions affect the specular reflectance and durability of the mirrors. Three anti-soiling coatings protect the mirrors from soiling phenomena, minimizing dust deposition and efficiency losses in CSP reflector plants.

4.1. Anti-Soiling Coating for CSP Reflector Mirrors

Hydrophobic Coatings: Hydrophobic or superhydrophobic coatings, often referred to as the "Lotus effect", feature high water contact angles and low surface energy, resulting in a self-cleaning effect [27]. A surface is considered hydrophobic if the water contact angle exceeds 90°, while it is superhydrophobic if the angle exceeds 150°, as shown in Figure 12. These surfaces minimize contact with the material's surface. Some available hydrophobic coatings include SiO_2, Al_2O_3, SnO_2, and silicate glasses. Silica-based coatings combined with fluoropolymers are commonly used as hydrophobic coatings to achieve the self-cleaning effect [28].

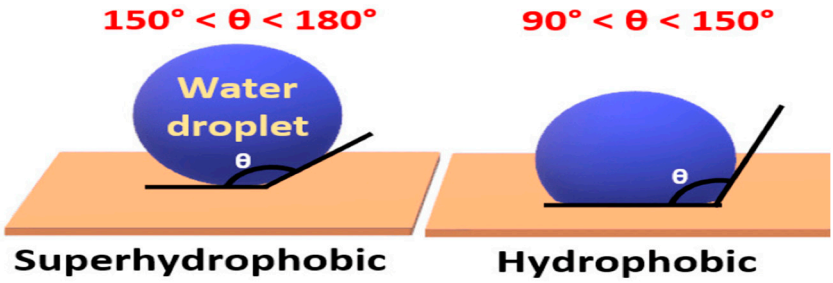

Figure 12. Superhydrophobic and Hydrophobic surfaces.

Hydrophilic Coatings: Hydrophilic or superhydrophilic surfaces have high surface energy and can maximize contact with the material and spread on the surface, especially with polar molecules. A surface is hydrophilic if its water contact angle is less than 90°. It is superhydrophilic if the angle is less than 45° (Figure 13). Superhydrophobic coatings can increase transparency and minimize dirt accumulation if the contact angle is less than 5° when the photo-catalytic property is activated [29].

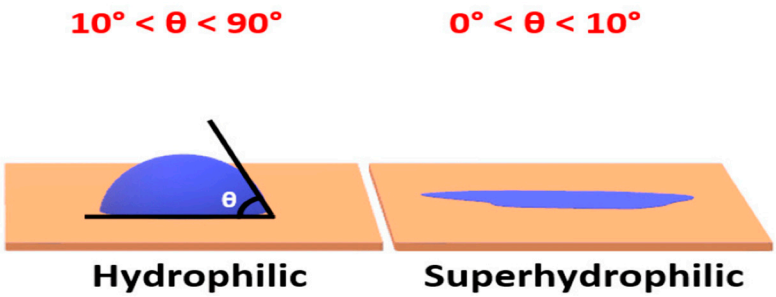

Figure 13. Hydrophilic and Superhydrophilic surfaces.

In addressing the effectiveness of hydrophobic and hydrophilic coatings in mitigating dust-related performance losses in PV systems, it is essential to consider their impact on dust accumulation and removal processes. Hydrophobic coatings reduce dust adhesion due to their low surface energy, which minimizes the contact area for dust particles. This property facilitates easier cleaning and maintenance of PV panels. In contrast, hydrophilic coatings, with their higher surface energy, enhance dust adhesion but may also aid in easier spread and wetting, potentially aiding in more efficient cleaning

methods. Understanding these coating properties and their influence on dust dynamics is crucial for optimizing PV system performance and longevity in dusty environments.

Photo-catalytic Super-hydrophilic Coatings: Photo-catalytic coatings based on transition metal oxides, such as TiO_2, ZnO, ZrO_2, and CeO_2, are effective in reducing dust and dirt on the surface of CSP reflectors [30]. Among these, TiO_2 has become a benchmark photo-catalyst due to its high transparency, chemical stability, and ability to break down organic matter into H_2O and CO_2 through the Honda–Fujishima effect [31].

4.2. Thermodynamics of Self-Cleaning Coating

Creating a self-cleaning effect on the surfaces of CSP reflector systems is crucial for minimizing dust adhesion and buildup, which in turn enhances the efficiency of the reflector mirrors

The self-cleaning effect of the surface is correlated with the water contact angle and surface energy. However, the wettability property depends on the chemical surface composition. Various methods are available to calculate the water contact angle of the surface, all of which are correlated with Young's Model, which calculates the contact angle of a droplet on a perfectly flat surface. On an ideal surface (smooth and homogeneous) [32], the contact angle is given by Young's equation:

$$\cos\theta_Y = \frac{\gamma_{SV}-\gamma_{SL}}{\gamma_{LV}} \quad (6)$$

where θ_Y is the contact angle on the solid surface, γ_{SV} represents the solid–vapor interface, γ_{SL} denotes the solid–liquid interface, and γ_{LV} pertains to the liquid interface.

As presented by Young's equation, the characterization of the surface suggests that there is contact in equilibrium. However, a hysteresis of the contact angle exists, as shown in Figure 14. The term "contact angle hysteresis" refers to observed differences between advancing and receding contact angles.

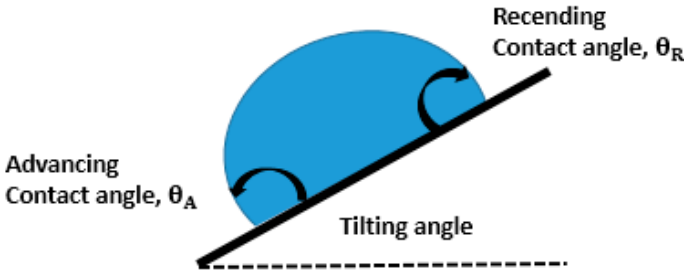

Figure 14. Contact angle hysteresis.

The below equation gives the contact angle hysteresis:

$$\Delta\theta = \theta_a - \theta_r \quad (7)$$

where θ_r is the receding contact angle, and θ_a is the advancing contact angle. Following the contact angle hysteresis, in 1962, Furmidge represented the hysteresis force per unit length required to anchor the water droplet on the surface [33]:

$$H = \frac{mg\sin\alpha}{w} = \gamma(\cos\theta_r - \cos\theta_a) \quad (8)$$

where α represents the minimum tilting angle required for the drop to slide, m denotes the mass of the drop, w indicates the width of the drop, and γ represents the surface tension between the liquid and air. The literature has shown that the leading causes affecting contact angle hysteresis are surface roughness and heterogeneities [14]. Without hysteresis, the contact angle value on the surface is handled by two primary models: the Wenzel model of 1936 and the Cassie and Baxter models of 1944. These models are based

on Young's equation. The Wenzel model takes into consideration geometric changes caused by surface roughness [34]. The surface area has a pronounced roughness, as shown in the following figure:

$$\cos\theta_w = r\cos\theta_Y = r\ \frac{\gamma_{SV}-\gamma_{SL}}{\gamma_{LV}} \quad (9)$$

where θ_w represents the apparent contact angle at stable equilibrium, θ_Y is the Young contact angle for an ideal surface, and **r** denotes the surface roughness, defined as the ratio of the actual surface area to the geometric surface area.

4.3. Surface Roughness Factor

The surface roughness factor is determined by dividing the real surface area by the geometric surface area, as illustrated in the Figure 15 [35].

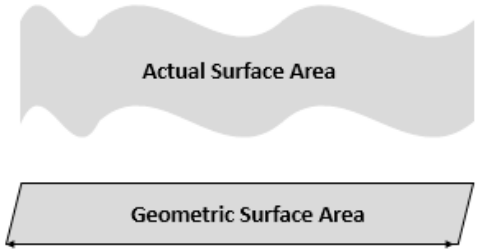

Figure 15. Surface roughness on the actual surface.

In addition to the Wenzel model, the Cassie and Baxter model's equation covers the phenomena of air pockets between a drop of liquid and surface depressions:

$$\cos\theta_{C-B} = r\cos\theta + r'\cos\theta' \quad (10)$$

where r is the solid surface fraction, and r' is the air surface fraction ($r + r' = 1$). When one of the surfaces is the air–liquid interface: $\theta' = 180$.

$$\cos\theta_{C-B} = -1 + r(1 + \cos\theta) \quad (11)$$

Therefore, augmenting the air surface fraction, associated with air pockets between a liquid drop and the surface, leads to hydrophobic properties on the surface. Figure 16 delineates the two models elucidating surface wettability.

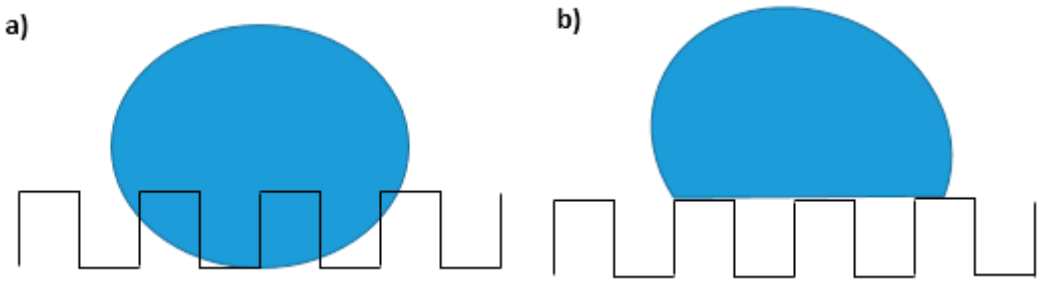

Figure 16. (**a**) Wenzel configuration and (**b**) Cassie and Baxter configuration.

For Wenzel's model, the increase in surface roughness amplifies the natural hydrophilicity or hydrophobicity of the material (more hydrophobic for hydrophobic surfaces and more hydrophilic for hydrophilic surfaces). So, since the system is in higher energy for hydrophobic surfaces, the Cassie and Baxter model proposes that the air may be pockets between a drop of liquid and the surface, as shown in Figure 16. The transition

criteria of the patterned surfaces for Cassie and Baxter's to Wenzel's model are discussed in the following section.

4.3.1. Cassie and Baxter to Wenzel Model Transition Criteria for Patterned Surfaces

Bharat Bhushan et al. [35] have demonstrated that a transition criterion has been developed to predict the shift from the Cassie–Baxter model to the Wenzel model. This transition was studied concerning dust traces on a surface after droplet evaporation [36]. Theoretically, this transition is described by considering a tiny water droplet on a superhydrophobic surface, as depicted in Figure 17. It has been demonstrated that the water droplet will remain suspended at the bottom of the cavities between the pillars. An alternative view of the droplet on the superhydrophobic surface is shown in Figure 18:

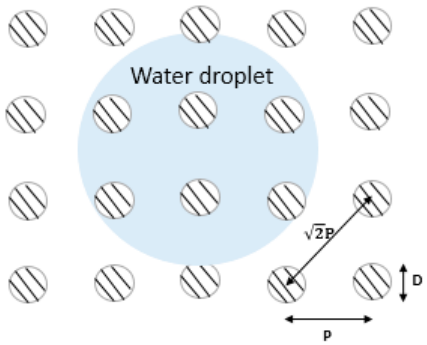

Figure 17. Water droplet on a superhydrophobic surface featuring a regular arrangement of circular pillars.

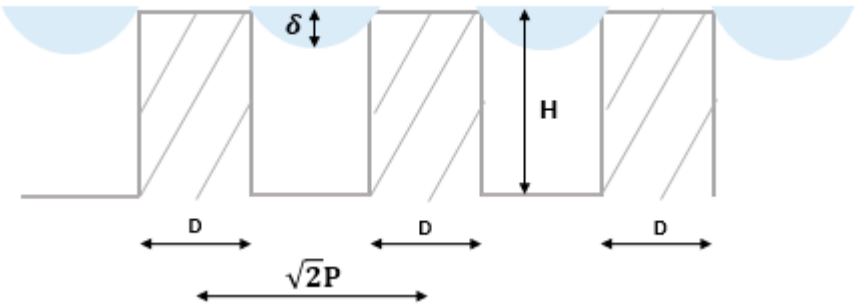

Figure 18. The maximum drop of a droplet (**δ**) between two pillars.

Where H is the height of the pillars, **P** is the pitch, and **D** is their diameter. The Laplace equation governs the curvature of a droplet, describing the relationship between its maximum drop (**δ**), pitch (**P**), and pillar height (**H**) [37]. If the droplet is far larger than the depth of the cavities, it will make contact with the bottoms of the cavities between the pillars, leaving no air behind. This causes a shift from the Cassie–Baxter model to Wenzel's model:

$$\boldsymbol{\delta} \approx \frac{(\sqrt{2}\boldsymbol{P}-\boldsymbol{D})^2}{\boldsymbol{R}} \quad (12)$$

if the greatest drop of a droplet is more than the height of pillars ($\boldsymbol{\delta} \geq \boldsymbol{H}$). So, there was no air pocket between them, causing the transition from the Cassie–Baxter to the Wenzel regime [38].

4.3.2. Surface Roughness Measurement

Surface roughness, a crucial aspect of surface texture, is quantified using various parameters, including arithmetic roughness (Ra) and root-mean-square roughness (Rq) [39]. These parameters can be computed along a profile line or across a surface area (Sa,

Sq). While profile line roughness metrics are more prevalent, area roughness parameters yield more significant insights. Several methods can gauge the surface roughness of a sample. Commonly utilized techniques in the literature include atomic force microscopy (AFM) and profilometry; although it is worth noting that AFM's measurement area is typically constrained [40]. The DektakXT stylus surface profiler is an advanced tool for measuring thin and thick film step heights, as shown in Figure 19. Alongside profiling surface topography and waviness, the DektakXT system provides roughness measurements, commonly expressed as Ra.

Figure 19. Image of a Stylus Profiler (DektakXT).

In a DektakXT stylus profiler, the stylus is mechanically connected to the core of an LVDT. The LVDT generates an analog signal proportional to the vertical stylus movement. This signal is amplified, conditioned, digitized, and saved for further processing, analysis, and presentation.

$$\mathbf{R_a} = \frac{\mathbf{1}}{\mathbf{L}} \int_{\mathbf{x=0}}^{\mathbf{x=L}} |\mathbf{y}| \mathbf{dx} \quad (13)$$

5. Dust Adhesion Measurements

Adhesion is typically described as the physical attraction between different substances. Particles adhere to surfaces due to the attractive forces between them and the substrate [41]. In our research, evaluating dust adhesion on CSP (concentrated solar power) reflector surfaces is essential for understanding how soiling affects solar mirrors and for identifying the most effective anti-soiling coatings to minimize dust accumulation on CSP systems, thereby enhancing their efficiency. The literature on dust adhesion includes various methods for assessing dust buildup on surfaces. This review covers different techniques for measuring dust adhesion. According to the surface free energy and extended DLVO theory, dust adhesion can be quantified using the Dupre or Hamaker equations [39]. Additionally, adhesion can be assessed by measuring adhesion forces and through atomic force microscopy (AFM), which provides precise measurements of adhesion at the micro- or nanoscale [40].

5.1. Dust Adhesion Measurement Based on Extended DLVO Theory

The DLVO theory, named after its originators Derjaguin, Landau, and Verwey, is a fundamental principle in colloid and interface science, as detailed by N.V. Churane [42]. Established in the 1940s, this theory describes the interactions between two surfaces by balancing two opposing forces: Van der Waals attraction and electrostatic repulsion. According to the DLVO theory, the total interaction free energy between two surfaces is determined by these competing forces. This theoretical framework offers a quantitative method for understanding adhesion and stability in colloidal systems and has been expanded to incorporate additional factors such as steric and hydration forces:

$$\boldsymbol{W(r)_{Total}} = \boldsymbol{W(r)_{VdW\ attract}} + \boldsymbol{W(r)_{electrostatic\ repuls}} \quad (14)$$

where $\boldsymbol{W(r)_{VdW\ attract}}$ represents the van der Waals attraction force and $\boldsymbol{W(r)_{electrostatic\ repuls}}$ presents the electrostatic force that is expressed by the Gouy–Chapman model as the following expression [43]:

$$\boldsymbol{W(r)_{electrostatic\ repuls}} = \frac{\boldsymbol{64\pi n_0 k_b T r_{sphere} \gamma^2 e^{-kr}}}{\boldsymbol{k^2}} \quad (15)$$

where $\boldsymbol{\gamma}$ is the reduced surface potential: $\boldsymbol{\gamma = \tanh\left(\frac{Ze\Psi}{4K_BT}\right)}$. Here, $\boldsymbol{\psi}$ is the potential on the surface, $\boldsymbol{n_0}$ is the number of ions present in the bulk (bulk ion concentration), $\boldsymbol{k_b}$ is the Boltzmann constant, $\boldsymbol{T}$ is the temperature in Kelvin, $\boldsymbol{r}$ is the intermolecular distance (Distance of Separation), $\boldsymbol{Z}$ is the valency of ions, $\boldsymbol{e}$ is the elementary charge, and $\boldsymbol{K}$ is the reciprocal of the Debye length. In the presence of water as a medium between two interaction surfaces, the classical DLVO theory does not consider polar or Lewis acid–base interactions. However, the total interaction free energy is then expressed by the extended DLVO theory [44], expressed as the following equation:

$$\boldsymbol{W(r)_{Total} = W(r)_{VdW\ attr} + W(r)_{elect\ rep} + W(r)_{Lewis\ interraction}} \quad (16)$$

In addition to the extended DLVO theory, in 1962, Fowkes proposed that the work of adhesion (W_{Adh}) between two interacting surfaces is presented by the equation [40]:

$$\boldsymbol{W_{Adh} = W^d_{Adh} + W^{nd}_{Adh}} \quad (17)$$

where $\boldsymbol{W^d_{Adh}}$ represents the dispersion interaction (or polar component), and $\boldsymbol{W^{nd}_{Adh}}$ represents the non-dispersion interaction (or nonpolar component).

All solids will have hydrophobic properties when the non-dispersion interactions' component is null. Non-dispersion interactions or nonpolar interactions include ionic bonding (Columbic interactions) and hydrogen bonding interaction. So, according to Bhattacharjee et al. [45], $\boldsymbol{W^{nd}_{Adh}}$ is null means that the solid's surface is free from any ionic or polar groups with which the water molecules can bond. According to Fowkes and Good van Oss's approaches, the surface free energy (SFE) of a solid is a sum of independent components associated with specific interactions:

$$\boldsymbol{\gamma_i = \gamma_i^d + \gamma_i^p + \gamma_i^h + \gamma_i^i + \gamma_i^{AB}} \quad (18)$$

where $\boldsymbol{\gamma^d_i}$, $\boldsymbol{\gamma^p_i}$, $\boldsymbol{\gamma^h_i}$, $\boldsymbol{\gamma^i_i}$ and $\boldsymbol{\gamma^{AB}_i}$ are the dispersion, polar, hydrogen bonding, induction, and acid-base components, respectively.

Fowkes primarily investigated systems with substances (solid or liquid) where only dispersion interactions are present. He associated dispersion interactions with London interactions, which arise from electron dipole fluctuations. The Owens–Wendt method, which deals with both polar and nonpolar interactions, simplifies the experiment by using contact angle measurements with two standard liquids of different polarities. This approach is commonly used to calculate the surface free energy (SFE) of polymeric materials. The Good–van Oss approach offers the most comprehensive description of the surface phenomena affecting SFE values. According to this approach, the dispersive component includes interactions from instantaneous dipoles, represented as γ^{LW}, and the polar component, γ^{AB}, is divided into acid (electron acceptor) and basic (electron donor) components:

$$\begin{cases} \boldsymbol{\gamma_S = \gamma_S^{LW} + \gamma_S^{AB}} \\ \boldsymbol{\gamma_L = \gamma_L^{LW} + \gamma_L^{AB}} \end{cases} \quad (19)$$

Or: $\boldsymbol{\gamma_L^{AB} = 2\sqrt{\gamma_L^+ \gamma_L^-}}$ and $\boldsymbol{\gamma_s^{AB} = 2\sqrt{\gamma_s^+ \gamma_s^-}}$

where $\boldsymbol{\gamma_s^+}$ represents the Lewis-acid component and $\boldsymbol{\gamma_s^-}$ represents the Lewis-base component. The polar component $\boldsymbol{\gamma^{AB}}$ of surface energy can exceed van der Waals components by up to two orders of magnitude and is most pronounced at distances less than 10 A°. Van der Waals interactions, while generally weaker than electrostatic interactions, exert influence over longer distances through $\boldsymbol{\gamma_S^{LW}}$ [46].

$$\gamma_{SL}^{Tot} = \gamma_S^{LW} + \gamma_L^{LW} - 2\sqrt{\gamma_L^{LW}\gamma_s^{LW}} + 2\left(\sqrt{\gamma_s^+\gamma_s^-} + \sqrt{\gamma_L^+\gamma_L^-} - \sqrt{\gamma_s^+\gamma_L^-} - \sqrt{\gamma_s^-\gamma_L^+}\right) \quad (20)$$

$$\gamma_{SV} = \gamma_{LV}\cos\theta_Y + \gamma_{SL} \quad (21)$$

By integrating the equations with Young's equation, we derive the subsequent equation employing the Good–van Oss methodology:

$$2\left\{\sqrt{\gamma_s^{LW}\gamma_L^{LW}} + \sqrt{\gamma_S^-\gamma_L^+} + \sqrt{\gamma_S^+\gamma_L^-}\right\} = \gamma_L(1 + \cos\theta_Y) \quad (22)$$

The surface free energy is determined by measuring the contact angles of three different liquids—neutral, polar, and nonpolar—each with known surface tension components [47]. The following system is then solved:

$$\begin{cases} 2\left\{\sqrt{\gamma_S^{LW}\gamma_{L1}^{LW}} + \sqrt{\gamma_S^-\gamma_{L1}^+} + \sqrt{\gamma_S^+\gamma_{L1}^-}\right\} = \gamma_{L1}(1 + \cos\theta_1) \\ 2\left\{\sqrt{\gamma_S^{LW}\gamma_{L2}^{LW}} + \sqrt{\gamma_S^-\gamma_{L2}^+} + \sqrt{\gamma_S^+\gamma_{L2}^-}\right\} = \gamma_{L2}(1 + \cos\theta_2) \\ 2\left\{\sqrt{\gamma_S^{LW}\gamma_{L3}^{LW}} + \sqrt{\gamma_S^-\gamma_{L3}^+} + \sqrt{\gamma_S^+\gamma_{L3}^-}\right\} = \gamma_{L3}(1 + \cos\theta_3) \end{cases} \quad (23)$$

5.2. Work of Adhesion

The work of adhesion refers to the reversible thermodynamic work required to separate the interface of two phases from equilibrium to an infinite separation distance. Hence, the work of adhesion is defined by the Dupre equation:

$$\Delta W_{12}^{adhesion} = \gamma_1 + \gamma_2 - \gamma_{12} \quad (24)$$

where γ_1 and γ_2 represent the surface energy of the reflector mirrors and dust particles, respectively, while γ_{12} denotes the interfacial surface energy between them. For a liquid–solid combination, the equation can be rewritten as:

$$\Delta W_{LS}^{adhesion} = \gamma_L + \gamma_S - \gamma_{LS} \quad (25)$$

where γ_L represents the liquid phase's surface tension, while γ_S represents the solid phase's surface energy, while γ_{LS} denotes the interfacial–surface tension between them. Similarly, the below equation represents the work of adhesion for three phases:

$$\Delta W_{132}^{adhesion} = W_{12}^a + W_{33}^a + \Delta W_{13}^a - W_{23}^a = \gamma_{13} + \gamma_{23} - \gamma_{12} \quad (26)$$

where $\Delta W_{132}^{adhesion}$ is the energy of cleaving the first phase from the second phase in a medium of the third phase [48]. As shown in Figure 20, we present an illustration of the cleavage following the two previous equations (Equations (25) and (26)):

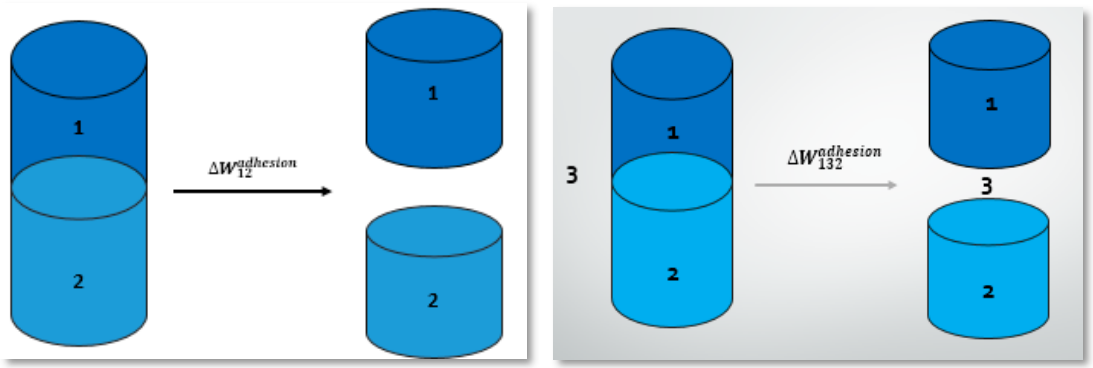

Figure 20. Illustration of the cleavage associated with the work of adhesion.

The work of adhesion is related to surface energy and tension. Understanding these notions is critical to comprehending the physical mechanisms of adhesion. Surface energy, or surface free energy, is the total of intermolecular forces at a material's surface and represents the work needed to form a new surface unit while separating two phases. Surfaces can be categorized by their surface energy into high or low. A low surface energy results in a high contact angle, indicating a hydrophobic surface, whereas a high surface energy results in a low contact angle, indicating a hydrophilic surface, as shown in Figure 21 [48]. In contrast, surface tension pertains to liquids and is defined as the property that enables the liquid surface to resist external forces.

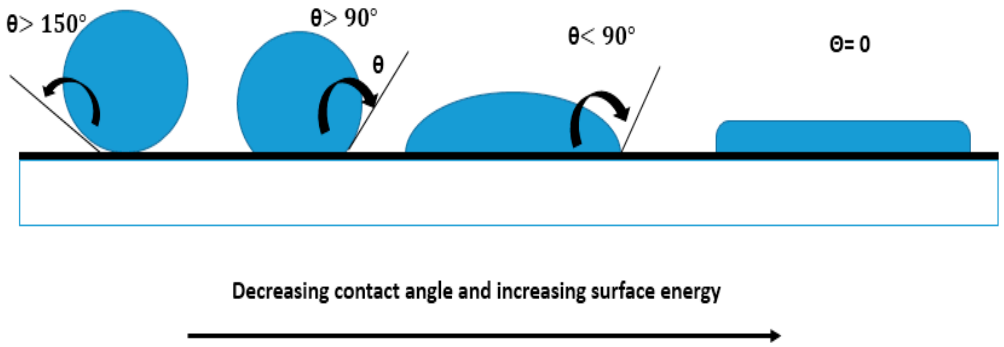

Figure 21. Illustration of the relationship between contact angle and surface energy.

5.3. Measurement of the Surface Energy and Surface Tension

Surface tension: The literature divides surface tension measurement techniques into two categories: static and dynamic approaches; the Du Nouy ring technique is one of the static methods available. The Du Nouy ring technique involved gradually lifting a platinum ring from the surface of a liquid, resulting in a force F that required elevating the ring from the liquid's surface and was proportional to the liquid's surface tension [49].

Surface energy: The sessile drop approach, illustrated in Figure 22, is the fundamental method for calculating the surface energy of a solid.

Figure 22. Measurement of contact angle using the sessile drop method.

This technique involves measuring the contact angle on the solid surface using three different liquids, neutral, polar, and nonpolar, each with known surface tension components [50].

5.4. Adhesion Forces

Four forces govern the dust adhesion on the solid surface. Van der Waal forces, capillary forces, electrostatic forces, and gravitational forces:

$$F_{Adh} = F_{VdW} + F_{Cap} + F_{el} + F_{gravity} \quad (27)$$

F_{vaw} is van der Waals, FCap is Capillary, Fel is Electrostatic, and Fgravity is Gravitational.

The gravitational forces are negligible for small particles with the size range of 1–500 μm. However, the following section presents an overview of all forces affected by dust particle adhesion.

Van der Waals (VDW) forces: VDW forces, also known as dispersion forces, are the attractive forces between any pair of atoms or molecules. Among various forces, van der Waals forces are particularly significant in dry conditions [48]. For instance, the van der Waals forces between a flat surface and a spherical particle can be described by the following equation:

$$F_{VdW} = \frac{AR}{6Z^2} \quad (28)$$

In this context, R represents the radius of the spherical particle, A denotes the Hamaker constant, and Z stands for the separation distance between a flat surface and a spherical particle. It is noteworthy that the separation distance typically ranges from 0.35 to 0.4 nm for an ideally smooth surface, whereas on other surfaces, such as those depicted in Figure 23, Z may range from 1 to 8 nm. Figure 24 visualizes the van der Waals force interaction between a flat surface and a spherical particle.

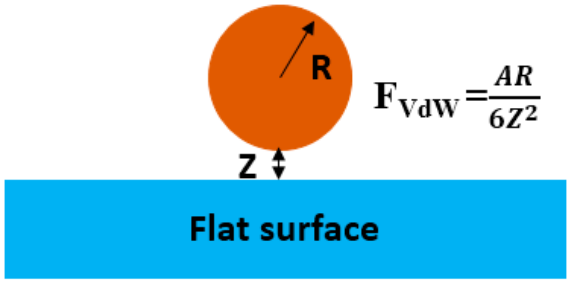

Figure 23. Illustration of van der Waals force between a flat surface and a spherical particle.

Capillary forces: Capillary force becomes predominant in high humidity conditions where water is present, leading to particle adhesion to the surface [51,52]. Similarly, like van der Waals force, the capillary force between a flat surface and a spherical particle can be described by the equation:

$$F_{Cap} = 4\pi R\gamma cos\theta \quad (29)$$

where R represents the radius of spherical particles, γ denotes the surface tension of water–air, and θ stands for the contact angle of water on the surface. Figure 24 illustrates the capillary force between a flat surface and a spherical particle.

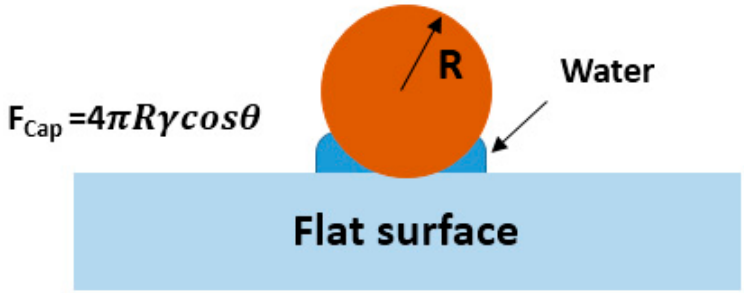

Figure 24. Illustration of capillary force on a flat surface.

Electrostatic forces: Electrostatic forces arise when dust particles gain an electric charge in the atmosphere through collisions. Even if the CSP reflector surfaces are not electrically charged, the charged particles will attract those with opposite charges, resulting in an electrostatic force on the surface [53]. This electrostatic force can be expressed by the following equation:

$$F_{el} = \frac{q^2}{4\pi\varepsilon\varepsilon_0 l^2} \quad (30)$$

where q is the charge of the particles, $\boldsymbol{\varepsilon}$ is the dielectric constant of the medium between the particle and the surface, $\boldsymbol{\varepsilon_0}$ is the permittivity of free space, and l is the separation distance between the charged particle and the flat surface.

Dust adhesion using AFM microscopy by Bruker (Billerica, MA, USA): In addition to the extended DLVO theory and the adhesion forces in the previous sections, the atomic force microscopy (AFM) technique is used to evaluate dust adhesion on the surface of solar panels. The following figure illustrates that the adhesion measurement can be evaluated by pushing or pulling the dust on the surface (the cantilever bows upward or down) [54].

As illustrated in Figure 25, the physical change caused by pushing or pulling dust can be attributed to the force holding the particle to the surface, allowing AFM microscopy to analyze dust particle adherence [54,55]. According to [41], AFM microscopy is inaccurate, expensive, and time-consuming.

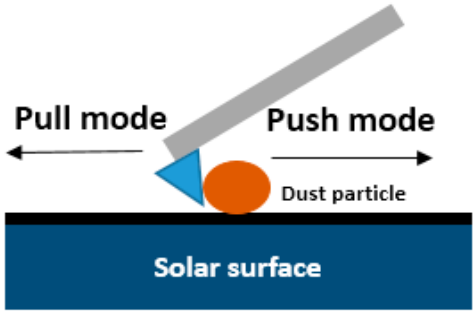

Figure 25. Illustration of AFM adhesion measurement.

Comparative Analysis of Dust Adhesion Measurement Techniques: In order to better understand different dust adhesion measurement methods and their application to CSP reflector surfaces we conducted a comparative study. The following tables summarize the main advantages and limitations of each method, providing insight into how it is appropriate to evaluate the associated dust in a CSP system. The most effective techniques for reducing and improving the operation and maintenance of CSP plants remains to be highlighted, as shown in Table 1.

Table 1. Comparative Analysis of Dust Adhesion Measurement Techniques.

Technique	Advantages	Limitations	Suitability for CSP Reflector Surfaces
Extended DLVO Theory	- Theoretical foundation for adhesion	- Requires accurate surface energy data - Assumes ideal conditions	- Provides a theoretical basis for understanding adhesion mechanisms but may not fully capture real-world conditions
Adhesion Force	- Quantifies individual forces (van der Waals, capillary, electrostatic) - Applicable to different particle sizes	- Complex calculations - Requires precise measurements of multiple parameters	- Useful for detailed analysis of dust adhesion dynamics - Can guide the development of tailored anti-soiling coatings
Atomic Force Microscopy	- High precision at micro/nano scale - Direct measurement of adhesion forces	- Expensive and time-consuming - Requires specialized equipment	- Suitable for detailed, high-resolution studies of dust adhesion on CSP surfaces - Can validate theoretical models

Monitoring and dust deposition based on OSM: As previously discussed, soiling measurements can be effectively performed using outdoor soiling microscopy (OSM), which analyzes images of soiled samples. This technique measures the deposition and removal of dust particles larger than 10 μm. Researchers at the Environment and Energy Research Institute in Qatar developed an OSM system with a small, low-power digital microscope connected to a Raspberry Pi3 for capturing and analyzing soiled images [56]. Dust accumulation on solar samples was assessed using ImageJ software from the OSM, allowing for the correlation of soiling rates with weather conditions.

Before concluding, it is worth describing strategies to address the challenges faced by CSP projects in the MENA region. Effectively addressing these challenges requires solutions that are sensitive to local environmental conditions and operational requirements. First, advanced anti-glare coatings adapted to the local climate hold the promise of reducing dust accumulation in sunglasses. These products have been developed to maintain high surface tension, reduce associated dust in dry areas, and improve optical performance. Routine cleaning and automated maintenance systems are needed to counter the adverse effects of dust deposition, in addition to ensuring continuous operation of CSP facilities, proper site selection and engineering design, considering existing ventilation systems and dust transport can reduce exposure to dusty environments.

Additionally, the combination of predictive maintenance technologies such as real-time monitoring systems and data-driven analytics enable better management of pollution challenges. This technology provides early warnings of visibility performance degradation due to dust accumulation, and facilitates timely intervention, planning, and maximizes uptime. By incorporating this strategic plan within the environment, we can meet the specific challenges in the MENA region and CSP projects can improve energy efficiency and make solar installations more efficient.

6. Conclusions

In conclusion, our study highlights the critical importance of addressing the impact of pollution on reflective lenses to improve the effectiveness of solar panels. By investigating dust adhesion mechanisms and the role of surface strength, we have highlighted the importance of soft-resistance coatings and advanced measurement techniques. Our findings highlight the need for tailored solutions that can adapt to different climatic conditions. Choosing the right CSP materials and implementing effective maintenance strategies are important steps to ensure the longevity and

performance of solar glasses. This review addresses practical challenges with solar implementation and promotes renewable energy solutions in the MENA region. Using these insights to drive innovation could pave the way for a brighter, cleaner solar-powered future.

Author Contributions: Methodology, A.E.B. and M.A.B.-M.K.; Software, A.E.B. and R.E.-n.; Validation, A.E.B. and A.K.; Formal analysis, A.J. and A.K.; Investigation, R.E.-n. and A.J.; Writing—original draft, A.E.B. and R.E.-n.; Writing—review & editing, R.E.-n. and M.A.B.-M.K.; Visualization, A.E.B., M.A.B.-M.K., A.J. and A.K. All authors have read and agreed to the published version of the manuscript.

Funding: This research received no external funding.

Institutional Review Board Statement: Not applicable.

Informed Consent Statement: Not applicable.

Data Availability Statement: Data are contained within the article.

Conflicts of Interest: The authors declare no conflict of interest.

References

1. Figgis, B.; Ennaoui, A.; Ahzi, S.; Rémond, Y. Review of pv soiling particle mechanics in desert environments. *Renew. Sustain. Energy Rev.* **2017**, *76*, 872–881.
2. Sayyah, A.; Horenstein, M.N.; Mazumder, M.K. Energy yield loss caused by dust deposition on photovoltaic panels. *Sol. Energy* **2014**, *107*, 576–604.
3. Wentworth, C.K. A scale of grade and class terms for clastic sediments. *J. Geol.* **1930**, *30*, 377–392.
4. Beaudoin, S.; Jaiswal, P.; Harrison, A.; Laster, J.; Smith, K.; Sweat, M.; Thomas, M. Fundamental forces in particle adhesion. *Part. Adhes. Remov.* **2015**, 1–79.
5. Kok, J.F.; Parteli, E.J.; Michaels, T.I.; Karam, D.B. The physics of wind-blown sand and dust. *Rep. Prog. Phys.* **2012**, *75*, 106901.
6. Ilse, K.; Khan, M.Z.; Voicu, N.; Naumann, V.; Hagendorf, C.; Bagdahn, J. Advanced performance testing of anti-soiling coatings—Part ii: Particle-size dependent analysis for physical understanding of dust removal processes and determination of adhesion forces. *Sol. Energy Mater. Sol. Cells* **2019**, *202*, 110049.
7. Reza, M.; Hizam, H.; Gomes, C.; Amran, M.; Ismael, M.; Hajighorbani, S. Power loss due to soiling on solar panel: A review. *Renew. Sustain. Energy Rev.* **2016**, *59*, 1307–1316.
8. Shag, A.; Yaping; Lu, H. A simple expression for wind erosion threshold friction velocity. *J. Geophys. Res.* **2000**, *105*, 437–443.
9. Chentouf, M.; Allouch, M. Environmental energy security in the MENA region–An aggregated composite index. *Environ. Dev. Sustain.* **2022**, *24*, 10945–10974.
10. Gokon, N. Progress in Concentrated Solar Power, Photovoltaics, and Integrated Power Plants Towards Expanding the Introduction of Renewable Energy in the Asia/Pacific Region. *Curr. Sustain. Renew. Energy Rep*. **2023**, *10*, 250–263.
11. Ilse, K.K.; Figgis, B.W.; Naumann, V.; Hagendorf, C.; Bagdahn, J. Fundamentals of soiling processes on photovoltaic modules. Renew. *Sustain. Energy Rev.* **2018**, *98*, 239–254.
12. Al-Hasan, A.Y.; Ghoneim, A.A. A new correlation between photovoltaic panel's efficiency and amount of sand dust accumulated on their surface. *Int. J. Sustain. Energy* 24, 187–197.
13. *IEC 61724-1*; Photovoltaic System Performance–Part 1: Monitoring. International Electrotechnical Commission: Geneva, Switzerland, 2017; Edition 1.0, 2017-03.
14. Griffith, D.J.; Vhengani, L.; Maliage, M. Measurements of mirror soiling at a candidate CSP site. *Energy Procedia* **2014**, *49*, 1371–1378.
15. Shuttleworth, R.; Bailey, G.L.J. The spreading of a liquid over a rough solid. *Discuss. Faraday Soc.* **1948**, *3*, 16–22.
16. Fernandez-Garcia, A.; Sutter, F.; Martinez-Arcos, L.; Sansom, C.; Wolfertstetter, F.; Delord, C. Equipment and methods for measuring reflectance of concentrating solar reflector materials. *Sol. Energy Mater. Sol. Cells* **2017**, *167*, 28–52.
17. Smestad, G.P.; Germer, T.A.; Alrashidi, H.; Fernández, E.F.; Dey, S.; Brahma, H.; Sarmah, N.; Ghosh, A.; Sellami, N.; Hassan, I.A.; et al. Modelling photovoltaic soiling losses through optical characterization. *Sci. Rep.* **2020**, *10*, 58.
18. Figgis, B.; Ennaoui, A.; Ahzi, S.; Rémond, Y. Review of pv soiling measurement methods. In Proceedings of the 2016 International Renewable and Sustainable Energy Conference (IRSEC), Marrakech, Morocco, 14–17 November 2016; pp. 176–180.
19. Figgis, B.; Ennaoui, A.; Guo, B.; Javed, W.; Chen, E. Outdoor soiling microscope for measuring particle deposition and resuspension. *Sol. Energy* **2016**, *137*, 158–164.
20. Lopes, D.; Concei, R.; Gon, H.; Aranzabe, E.; G. Pérez; Collares-Pereira, M. Anti-soiling coating performance assessment on the reduction of soiling effect in second-surface solar mirror. *Sol. Energy* **2019**, *194*, 478–484.
21. Bethea, R.M.; Barriger, M.T.; Williams, P.F.; Chin, S.; Solar, C.; Project, P. Environmental effects on solar concentrator mirrors. *Sol. Energy* **1981**, *27*, 497–511.
22. Kennedy, C.E. Optical durability of candidate solar reflectors. *ASME Trans.* **2016**, 1–10.

23. Pina, A. Technical evaluation of an improved paint coating with nir pigments designed to reduce incident solar radiation: Application in the caribbean area. *Energy Procedia* **2017**, *115*, 463–479.
24. Aytac, T.; Barshan, B. Surface differentiation by parametric modeling of infrared intensity scans. *Opt. Eng.* **2005**, *44*, 067202.
25. Garcia-Segura, A.; Fern, A.; Ariza, M.J.; Sutter, F.; Valenzuela, L. Durability studies of solar reflectors: A review. *Renew. Sustain. Energy Rev.* **2016**, *62*, 453–467.
26. Schissel, P. Silvered-pmma reflectors. *Sol. Energy Mater. Sol. Cells* **1994**, *33*, 183–197.
27. Asmatulu, R.; Khan, W.S.; Reddy, R.J.; Ceylan, M. Synthesis and Analysis of Injection-Molded Nanocomposites of Recycled High-Density Polyethylene Incorporated with Graphene Nanoflakes Department of Mechanical Engineering. *Polym. Compos.* **2015**, *36*, 1565–1573.
28. Almanza, R.; Herna, P. Development and mean life of aluminum first-surface mirrors for solar energy applications. *Sol. Energy Mater. Sol. Cells* **2009**, *93*, 1647–1651.
29. Latthe, S.S.; Sutar, R.S.; Kodag, V.S.; Bhosale, A.K.; Kumar, A.M. Self-cleaning superhydrophobic coatings: Potential industrial applications. *Prog. Org. Coat.* **2019**, *128*, 52–58.
30. Kulinich, S.A.; Farzaneh, M. Hydrophobic properties of surfaces coated with fluoroalkylsiloxane and alkylsiloxane monolayers. *Surf. Sci.* **2004**, *573*, 379–390.
31. Fujishima, A.; Rao, T.N.; Tryk, D.A. Titanium dioxide photocatalysis. *J. Photochem. Photobiol. C Photochem. Rev.* **2000**, *1*, 1–21.
32. Carrier, O.; Bonn, D. *Droplet Wetting and Evaporation*; Number 1950; Elsevier Inc.: Amsterdam, The Netherlands, 2015.
33. Furmidge, C. Studies at phase interfaces. i. the sliding of liquid drops on solid surfaces and a theory for spray retention. *J. Colloid Sci.* **1962**, *17*, 309–324.
34. Marmur, A. Wetting on hydrophobic rough surfaces: To be heterogeneous or not to be? *Langmuir* **2003**, *1*, 8343–8348.
35. Jung, Y.C.; Bhushan, B. Wetting transition of water droplets on superhydrophobic patterned surfaces. *Scr. Mater.* **2007**, *57*, 1057–1060.
36. Mchale, G.; Aqil, S.; Shirtcliffe, N.J.; Newton, M.I.; Erbil, H.Y. Analysis of droplet evaporation on a superhydrophobic surface. *Langmuir* **2005**, *21*, 11053–11060.
37. Lafuma, A.; Quéré, D. Superhydrophobic states. *Nat. Mater.* **2003**, *2*, 457–460.
38. Techniques, A. Promising future processing technology promising future processing technology. In *Advances in CMP Polishing Technologies*; William Andrew: Norwich, NY, USA, 2012; pp. 229–295.
39. Quesnel, D.J.; Zeng, X.; Renshaw, P.F.; Helms, C.A.; Grisham, A.; Chin, J.; Fellers, T.; Lai, F.; Yoon, J.; Torralba, S.; et al. Aspects of particle adhesion and removal. In *Developments in Surface Contamination and Cleaning*, 2nd ed.; Elsevier Inc.: Amsterdam, The Netherlands, 2016; Volume 1, pp. 119–146.
40. Isaifan, R.J.; Johnson, D.; Ackermann, L.; Figgis, B.; Ayoub, M. Evaluation of the adhesion forces between dust particles and photovoltaic module surfaces. *Sol. Energy Mater. Sol. Cells* **2019**, *191*, 413–421.
41. Zafar, U.; Hare, C.; Hassanpour, A.; Ghadiri, M. Drop test: A new method to measure the particle adhesion force. *Powder Technol.* **2014**, *264*, 236–241.
42. Kazmerski, L.L.; Diniz, A.S.A.; Maia, C.B.; Viana, M.M.; Costa, S.C.; Brito, P.P.; Campos, C.D.; Neto, L.V.M.; de Morais Hanriot, S.; de Oliveira Cruz, L.R. Fundamental studies of adhesion of dust to PV module surfaces. *IEEE J. Photovolt.* **2016**, *6*, 719–729.
43. Tan, C.L.C.; Gao, S.; Wee, B.S.; Asa-Awuku, A.; Thio, B.J.R. Adhesion of dust particles to common indoor surfaces in an air-conditioned environment. *Aerosol. Sci. Technol.* **2014**, *6826*, 541–551.
44. Churaev, N.V. The dlvo theory in russian colloid science. *Adv. Colloid Interface Sci.* **1999**, *83*, 19–32.
45. Bhattacharjee, S.; Elimelech, M.; Borkovec, M. Dlvo interaction between colloidal particles: Beyond derjaguin's approximation. *Croat. Chem. Acta* **1998**, *71*, 5–8.
46. Laskowski, J.; Kitchener, J.A. The hydrophilic–hydrophobic transition on silica. *J. Colloid Interface Sci.* **1968**, *29*, 670–679.
47. Van Oss, C.J.; Chaudhury, M.K.; Good, R.J. Interfacial lifshitz-van der Waals and polar interactions in macroscopic systems. *Chem. Rev.* **1988**, *88*, 927–941.
48. Chan, C.T.; Ho, K.M.; Bohnen, K.P. Surface reconstruction: Metal surfaces and metal on semiconductor surfaces. *Phys. Struct.* **1996**, *1*, 101–136.
49. Marshall, S.J.; Bayne, S.C.; Baier, R.; Tomsia, A.P.; Marshall, G.W. A review of adhesion science. *Dent. Mater.* **2010**, *6*, 11–16.
50. Is, W.; Interface, A.N.; Tension, S. Surface tension and its measurement. In *Adhesives Technology Handbook*; William Andrew Publishing: Norwich, NY, USA, 2015; pp. 19–34.
51. Rifai, A.; Abu, N.; Yilbas, B.S.; Khaled, M. Mechanics of dust removal from rotating disk in relation to self-cleaning applications of PV protective cover. *Sol. Energy* **2016**, *130*, 193–206.
52. Quan, Y.; Zhang, L.; Qi, R.; Cai, R. *Self-Cleaning of Surfaces: The Role of Surface Wettability and Dust Types*; Nature Publishing Group: Berlin, Germany, 2016; pp. 1–12.
53. Butt, H.; Kappl, M. Normal capillary forces. *Adv. Colloid Interface Sci.* **2009**, *146*, 48–60.
54. Bowling, R.A. An analysis of particle adhesion on semiconductor surfaces. *J. Electrochem. Soc.* **1985**, *157*, 2208–2214.

55. Alexander, S.; Hellemans, L.; Marti, O.; Schneir, J.; Elings, V.; Hansma, P.K.; Longmire, M.; Gurley, J. An atomic-resolution atomic force microscope implemented using an optical lever. *J. Appl. Phys.* **1989**, *65*, 164–167.
56. Bhushan, B.; Marti, O. Scanning probe microscopy–principle of operation, instrumentation, and probes. In *Nanotribology and Nanomechanics*; Springer: Cham, Switzerland, 2011; pp. 37–110.